SCIENTIFIC REP🅞RTS

OPEN

Spin-dependent thermoelectric effects in Fe-C$_6$ doped monolayer MoS$_2$

Lin Zhu, Fei Zou, Guoying Gao & Kailun Yao

By using the non-equilibrium Green's function with density functional theory, we have studied the thermal spin transport properties of Fe-C$_6$ cluster doped monolayer MoS$_2$. The results show that the device has a perfect Seebeck effect under temperature difference without gate voltage or bias voltage. Moreover, we also find the thermal colossal magnetoresistance effect, which is as high as 10^7%. The competition between spin up electrons and spin down holes of the parallel spin configuration leads to peculiar behavior of colossal magnetoresistance and thermo-current, which is essential for the design of thermal transistors. These results are useful in future MoS$_2$-based multifunctional spin caloritronic devices.

Spin caloritronics aims to explore the coupling and application of spins and charges with heat currents in materials[1], which has potential applications in future technologies, such as green energy and information science. Encouraged by experimentally inversing spin Hall effect (ISHE)[2–4] based physical measurements, spin caloritronics should treat an invigorated intersection of spintronics and thermoelectronics. Especially, unlike the spin polarized current relying on the bias voltage in spintronics, the thermally induced spin current is just generated from a temperature gradient, instead of electrical bias. In the field, spin Seebeck effect (SSE) is an inspiring discovery in ferromagnetic metal and semiconductor et al.[5–9], which can achieve a conversion between heat and electricity, then provides an effective way and a new direction to explore and utilize new materials and green energy. Moreover, if spin-up and spin-down thermo-currents with nearly equal magnitudes flow in opposite directions, the perfect SSE occurs. Perfect SSE devices allow us to obtain the net spin current, decreasing dissipation heat caused by the total charge current. Therefore, we can design low-power consumption devices based on spin caloritronics. However, a huge challenge to realize the perfect SSE is to search the good spin caloritronic material.

The monolayer MoS$_2$ and the related two-dimensional materials exhibit superior caloritronic performance[10–12], they have attracted much attention[13–15]. Different from graphene and silicene, monolayer MoS$_2$ has a direct energy gap of 1.8 eV[16, 17]. When transition metal atom is doped, the dopant 3d states present in the energy gap, then the magnetism of the doped system can be controlled by regulating 3d states of transition metal. Recent experiments successfully doped transition metals in monolayer MoS$_2$[18]. There are also some theoretical studies on transition metals or atomic clusters doped monolayer MoS$_2$[19–22]. Cheng et al.[19] used the first-principles method to predict that the two-dimensional dilute magnetic semiconductors (DMSs) were easy to achieve by substitution of Mo with Mn, Fe, Co or Zn atom in monolayer MoS$_2$. Feng et al.[21] considered that the six S atoms in the vicinity of Mo could be replaced by other non-metallic elements (such as C, O, etc.), and they doped monolayer MoS$_2$ with Fe-C$_6$ and Fe-O$_6$ clusters acquiring two DMSs. The devices based on MoS$_2$ had also been designed[23–31].

Here, we proposed a Fe-C$_6$ cluster doped monolayer MoS$_2$ system with an intriguing thermally induced colossal magneto-resistance (CMR) without gate voltage, finding the negative thermal magnetoresistance. Meanwhile, the perfect SSE and nonlinear response behavior of charge current were also observed.

Model and Methods

The model device displayed in Fig. 1 was divided into three parts: the left and right electrodes, and the scattering region. A $4 \times 4 \times 1$ supercell model by replacing Mo-S$_6$ with Fe-C$_6$ was built. For convenience, we label the device with the symbol Fe-C$_6$.

The transport calculations were performed within the framework of the QuantumWise ATK package[32–34]. The Perdew-Burke-Ernzernhof (PBE)[35] spin-polarized generalized gradient approximation (SGGA) was used for the

School of Physics and Wuhan National High Magnetic Field Center, Huazhong University of Science and Technology, Wuhan, 430074, China. Correspondence and requests for materials should be addressed to L.Z. (email: linzh@hust.edu.cn)
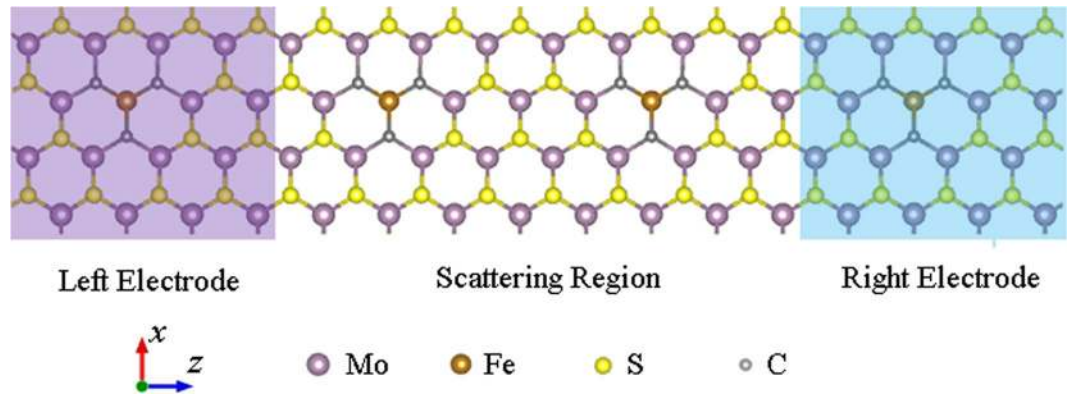
Figure 1. Schematic illustration of two-probe system. Schematic illustration of Fe-C_6 cluster doped monolayer MoS_2 two-probe system.

exchange-correlation potential, and the valence electronic orbitals were expanded in double-polarized basis set. The thermally induced current was given by[36]

$$I^\sigma = \frac{e}{h} \int_{-\infty}^{+\infty} \{T^\sigma(E)[f_L(E, T_L) - f_R(E, T_R)]\}dE \tag{1}$$

here σ ($=\uparrow, \downarrow$) denotes the spin index, and $\mu_{L/R}$ is the electrochemical potential for source/drain. As we just considered the temperature difference without gate voltage or bias voltage, then $\mu_L = \mu_R = E_F$ (Fermi level) was set to zero. $T^\sigma(E) = Tr(\Gamma_L G^R \Gamma_R G^A)^\sigma$ is spin-resolved transmission function.

The system was relaxed sufficiently till the maximum force dropped below a threshold value of 0.01 eV/Å. Experimentally, the magnetization of the left and right electrodes can be aligned in parallel (P) or antiparallel (AP) spin configuration by a sufficiently strong external magnetic field. Therefore, the P and AP spin configurations were both considered. The total energy of AP spin configuration was 0.88 meV less than that of the P spin configuration per unit cell.

Results and Discussion

Figure 2 displays the thermally induced currents of Fe-C_6 device *versus* T_L with different ΔT ($\Delta T = T_R - T_L$), and these *versus* ΔT at different T_L for P spin configuration. The trend of curve is almost identical for spin-up or spin-down state, and there are no temperature threshold. The spin-polarized currents increase rapidly in low T_L region and slowly in high T_L region for all ΔT (Fig. 2(a)), but the currents almost linearly increase in the whole range of ΔT for all T_L (Fig. 2(b)). The different sign of spin-up and spin-down currents implies SSE.

We now discuss the charge currents I_C ($I_{up} + I_{dn}$) and spin currents I_S ($I_{up} - I_{dn}$) as a function of T_L to describe the SSE. As can be seen from Fig. 3, I_S is about 10 times larger than I_C for each of ΔT. When ΔT ranges from 20 K to 60 K, I_S increases. It is noteworthy that I_C shows unusual behavior. We take $\Delta T = 60$ K as an example. As T_L increases, I_C declines to negative value, and reaches to its minimum -0.7 nA at $T_L = 100$ K, after that, I_C begins to increase to almost zero (about -0.09 nA) at 140 K. Whereafter, I_C continues to increase with increasing T_L, and finally reaches the maximum value 7.21 nA at $T_L = 370$ K, then decreases again. The novel property of I_C is due to the competition between I_{up} and I_{dn}, videlicet, the result of the competition between the spin up hole carriers and the spin down electron carriers in the heat transport. The nonlinear response of I_C is very necessary for the design of thermal transistors. At $\Delta T = 60$ K, $T_L = 140$ K, the value of I_C is -0.09 nA, but I_S is -8.87 nA. Although at $T_L = 150$ K, I_C is very small (0.24 nA), but the absolute value of I_S is also large ($I_S = -44.62$ nA). The above results indicate that the net spin current is produced at $\Delta T = 60$ K within the T_L region (140 K, 150 K), and the total charge current is well suppressed. Thus the perfect SSE occurs.

Here, the electrode leads are the same material, and the left electrode is colder than the right electrode. When the source and drain have different temperature, the behavior of carrier is determined not only by transmission function, but also by the Fermi distribution difference $f_L(E, T_L) - f_R(E, T_R)$ which is only related to the temperature $T_{L/R}$ of source/drain. If the transmission functions of spin-up and spin-down channels are strong symmetric around Fermi level, the electron current (I_e) and hole current (I_h) will be cancelled each other and the device will not have total charge current, only net spin current is produced. In Fe-C_6 device, the spin down carriers (electrons) flow from drain to source, producing the positive current, while the current generated by the spin-up carriers (holes) flowing from source to drain is negative, then there is a nonzero spin current in the P configuration.

To elucidate the physical mechanism for SSE, we analyze the band structure of Fe-C_6 doped monolayer MoS_2 system and the spin dependent transmission function of Fe-C_6 device, as shown in Fig. 4(a). The mechanism of the current generated from temperature difference credits to the electron band structure. The left panel of Fig. 4(a) manifests that the spin-up and spin-down bands are split and have a good symmetry near the Fermi level, thus the Fe-C_6 doped system is a spin semiconductor. The transmission function (the middle panel of Fig. 4(a)) shows that the spin-up and spin-down transport channels are both opened near the Fermi level for P spin configuration, due to the match of the bands of the left and right electrode. Accordingly, transmission peaks near the Fermi level present in the energy range $(-0.124 \text{ eV}, -0.045 \text{ eV})$ and $(0.055 \text{ eV}, 0.114 \text{ eV})$ for spin-up and
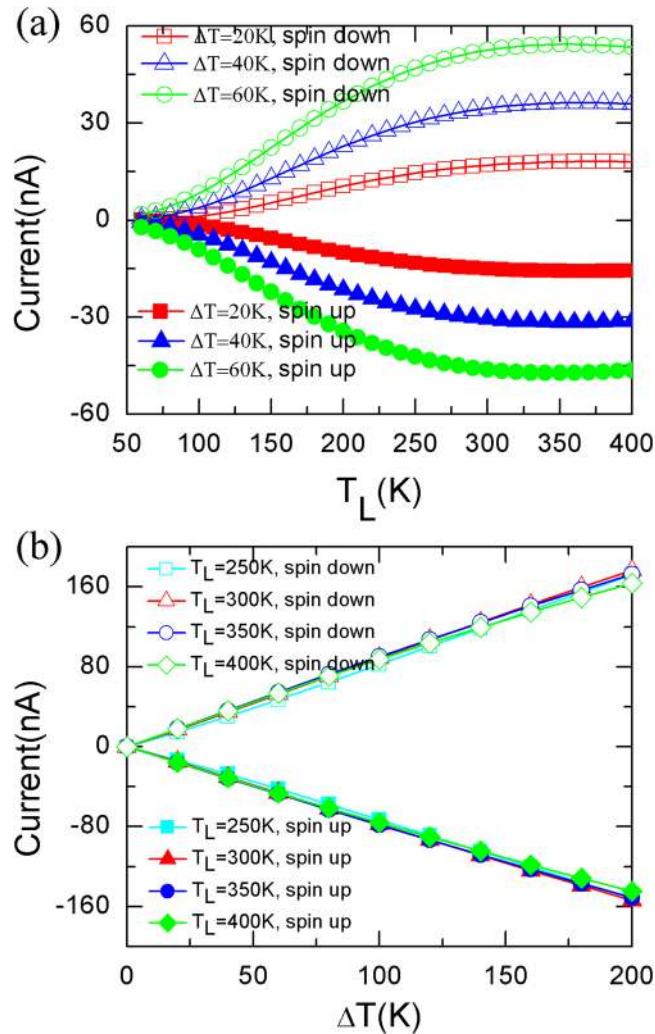
Figure 2. The spin-resolved thermal current. The spin-dependent thermal currents *versus* T_L for different ΔT ($\Delta T = T_R - T_L$) (**a**) and *versus* ΔT for different T_L (**b**) for P spin configuration.

spin-down channels, respectively. Because they are very close to the Fermi level, the temperature threshold is small. These two peaks break the electron-hole symmetry in the transmission function, resulting in the nonzero net thermal spin currents. Additionally, the transmission peaks of both channels are almost symmetrical about the Fermi level, thereby, Fe-C_6 device produces a perfect SSE. The spin splitting of the density of states (DOS) in Fig. 4(b) verifies the spin-polarized transport. Furthermore, the spin up and down DOS are nearly symmetric about the Fermi level, therefore, there should be SSE. The lower panel of Fig. 4(b) reveals that it is the *d*-states of Fe, *p*-states of the nearest neighbor C, and *d*-states of the second-nearest neighbor Mo contributing to the thermal transport properties.

Now, we analyze the current spectra ($J(E) = T(E)(f_L(E, T_L) - f_R(E, T_R))$) (Fig. 4(c)), which reflects the value of current. The spin-up and spin-down current spectra both augment with the increasing of T_L or ΔT, and they are almost equal in area, resulting in numerically approximate equal of spin up and spin down currents with opposite signs. These phenomena further confirm the emergence of SSE.

When the device is transformed from P spin configuration to AP spin configuration, the CMR effect of the device appears, $MR(\%) = (I_C^P - I_C^{AP})/I_C^{AP} \times 100$. Figure 5(a) display that the total charge current of AP spin configuration (I_C^{AP}) is smaller than that of P spin configuration (I_C^P), owing to the transport channel of P spin configuration is closer to the Fermi level than that of AP spin configuration. I_C^P changes from negative value to positive value with increasing T_L, but its absolute value at most T_L points is much larger than I_C^{AP}. Figure 5(b) denotes that the CMR reaches $10^7\%$ (or $-10^7\%$) in wide range of T_L and is accompanied by the change of symbol, which has special significance and will be widely used in the logic devices. The reason for above phenomenon is that I_C^P varies from negative to positive sign with increasing T_L (see Fig. 5(a)) and is much larger than I_C^{AP} which is negative and almost zero, thus positive and negative magnetoresistances emerge as indicated by the insert of Fig. 5(b).

The thermal magneto-resistance behavior of Fe-C_6 doped MoS_2 is very similar to that of Fe-doped MoS_2[37], but the mechanism is disparate. The negative magnetoresistance of Fe-C_6 doped MoS_2 system is the result of
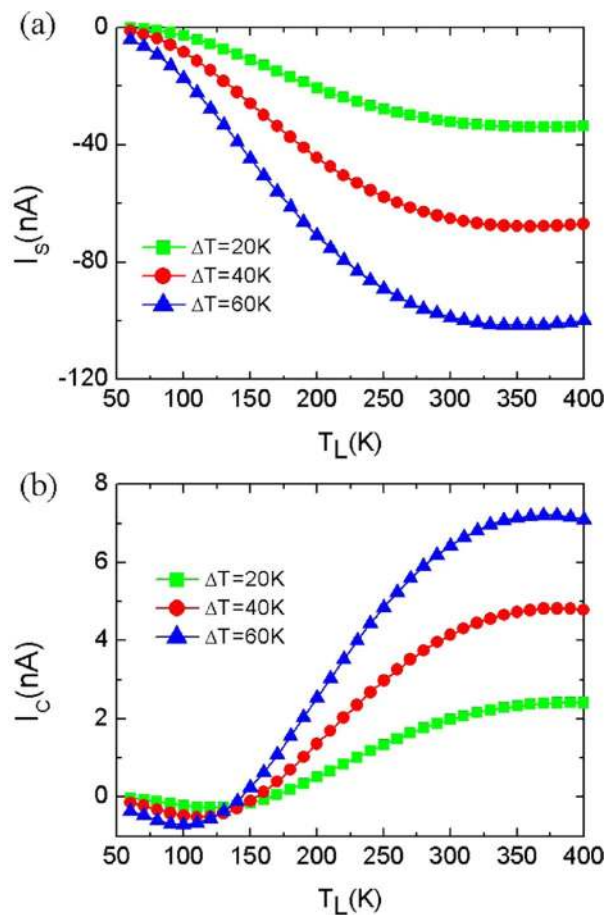
Figure 3. The total charge current and net spin current. The total charge current I_C $(I_{up} + I_{dn})$ (**a**) and the net spin current I_S $(I_{up} - I_{dn})$ (**b**) of Fe-C$_6$ device as a function of T_L for P spin configuration.
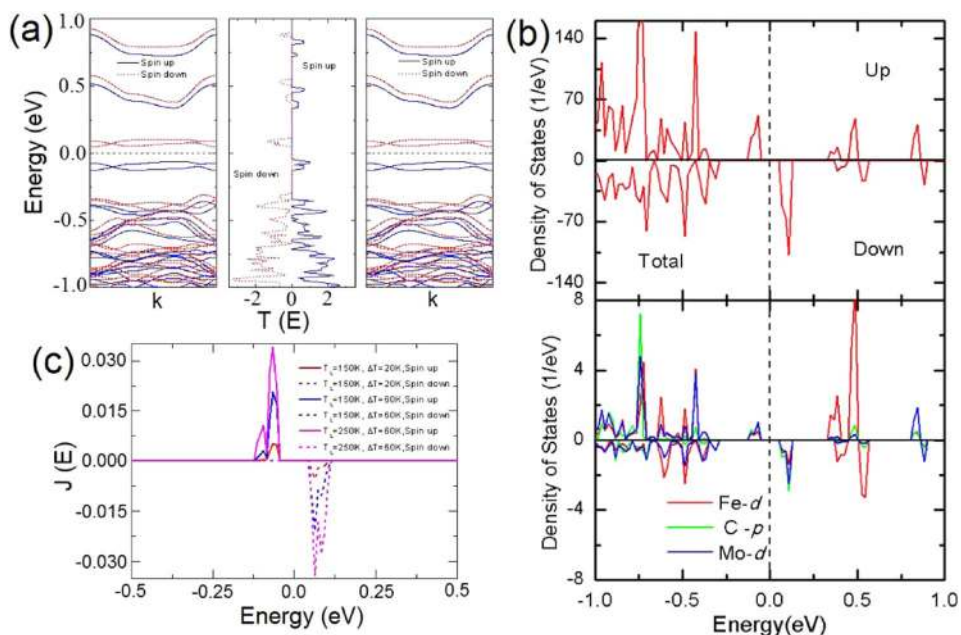

Figure 4. The spin-resolved electronic structures and the current spectra. (**a**) Band structures of electrode (the left panel is the same as the right one) and the spin-polarized transmission spectrum for P (middle panel) spin configuration. (**b**) The electronic structures for Fe-C$_6$ device and atomic orbital. (**c**) Spin-polarized current spectra for various T_L and ΔT.
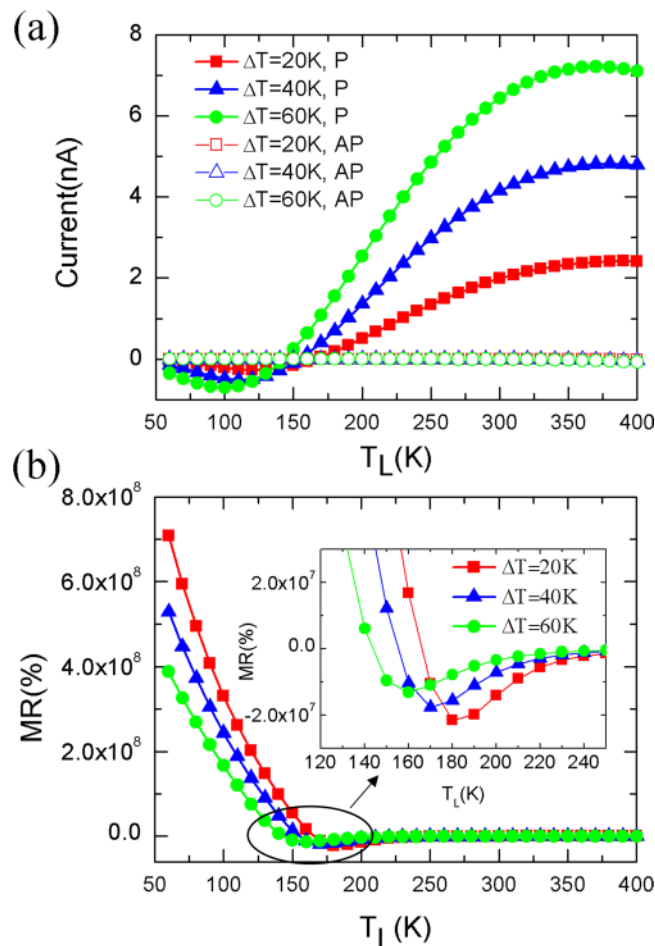
Figure 5. The total charge current and the thermal magnetoresistance. (**a**) The total charge current as a function of T_L for P and AP spin configurations with $\Delta T = 20$, 40 and 60 K. (**b**) The thermal magnetoresistance as a function of T_L. For clarity, the inset shows the magnetoresistance at the flex point with a smaller scale.

competition between spin up holes and spin down electrons of P spin configuration. The negative magnetoresistance of Fe-doped MoS_2 system is caused by the sign change of total charge current of AP spin configuration[37]. The CMR shows a strong regularity within several ΔT and its value gradually moves close to zero until finally reaches to -10^4% in Fe-C_6 device. For convenience, we also call the negative magnetoresistance phenomenon 'Zigzag'. The behavior of 'Zigzag' shifts to low T_L with increasing ΔT. Negative magnetoresistance appears in the lower T_L with a higher ΔT, which is in agreement with that of Fe-doped MoS_2 system. However, the maximum negative magneto-resistance value begins to increase when ΔT decreases. Namely, the magnetoresistance of $\Delta T = 60$ K is less than that of $\Delta T = 40$ K, which is also less than that of $\Delta T = 20$ K. Based on temperature difference and magnetic field, one can control carriers transport to change the magnetoresistance of Fe-C_6 doped monolayer MoS_2 two-probe system, the thermal CMR is higher than 10^7% and accompanied with the conversion between negative value and positive value. Our findings may provide a good reference to experiment.

We also consider the size effect on the thermally transport. For P spin configuration, the phenomenon of the thermal transport is almost not affected by the length of the scattering region, and the perfect SSE arises yet. The tendency of thermally induced CMR is not changed when T_L increases, but in many of the T_L points, its values augment nearly two orders of magnitude when the length of the scattering region is enlarged from two doped units to four doped units, reaching 10^{10}% because of the decrease of I^{AP}. Meanwhile, the 'zigzag' phenomenon of CMR still exists. It can be concluded that the thermal transport properties are enhanced by aggrandizing the length of scattering region.

Conclusions

In conclusion, a new configuration of spin caloritronic device based on Fe-C_6 cluster doped monolayer MoS_2 was presented, and its thermal transport properties had been investigated by NEGF-DFT approach. Spin-polarized currents can be produced only by applying temperature gradient between the left and the right electrodes. The SSE is observed in the thermal electron current. An intriguing thermally induced CMR without gate regulating occurs in the device, which has different sign in distinct T_L region while ΔT is fixed. The peculiar behavior of CMR and the nonlinear response regime of I_c arise from the competition between spin-up electrons and spin-down holes of

the P spin configuration. Additionally, we find that the thermal transport properties of enlarged scattering region are enhanced. The results manifest that the MoS_2-based materials have potential application in spin caloritronics and spintronics.

References

1. Bauer, G. E., Saitoh, E. & van Wees, B. J. Spin caloritronics. *Nat. Mater.* **11**, 391–399 (2012).
2. Saitoh, E., Ueda, M., Miyajima, H. & Tatara, G. Conversion of spin current into charge current at room temperature: Inverse spin-Hall effect. *Appl. Phys. Lett.* **8**, 182509 (2006).
3. Valenzuela, S. O. & Tinkham, M. Direct electronic measurement of the spin Hall effect. *Nature* **442**, 176–179 (2006).
4. Kimura, T., Otani, Y., Sato, T., Takahashi, S. & Maekawa, S. Room-temperature reversible spin Hall effect. *Phys. Rev. Lett.* **98**, 156601 (2007).
5. Uchida, K. *et al.* Observation of the spin Seebeck effect. *Nature* **455**, 778–781 (2008).
6. Jaworski, C. M. *et al.* Observation of the spin-Seebeck effect in a ferromagnetic semiconductor. *Nat. Mater.* **9**, 898–903 (2010).
7. Bosu, S. *et al.* Spin Seebeck effect in thin films of the Heusler compound Co_2MnSi. *Phys. Rev. B* **83**, 224401 (2011).
8. Uchida, K. *et al.* Spin Seebeck insulator. *Nat. Mater.* **9**, 894–897 (2010).
9. Jaworski, C. M., Myers, R. C., Johnston-Halperin, E. & Heremans, J. P. Giant spin Seebeck effect in a non-magnetic material. *Nature* **487**, 210–213 (2012).
10. Zhang, G. & Zhang, Y. W. Strain effects on thermoelectric properties of two-dimensional materials. *Mech. Mater.* **91**, 382 (2015).
11. Cai, Y. Q., Lan, J. H., Zhang, G. & Zhang, Y. W. Lattice vibrational modes and phonon thermal conductivity of monolayer MoS_2. *Phys. Rev. B* **89**, 035438 (2014).
12. Wei, X. L. *et al.* Phonon thermal conductivity of monolayer MoS_2: A comparison with single layer graphene. *Appl. Phys. Lett.* **105**, 103902 (2014).
13. Fan, D. D. *et al.* MoS_2 nanoribbons as promising thermoelectric materials. *Appl. Phys. Lett.* **105**, 133113 (2014).
14. Liu, X., Zhang, G., Pei, Q.-X. & Zhang, Y.-W. Phonon thermal conductivity of monolayer MoS_2 sheet and nanoribbons. *Appl. Phys. Lett.* **103**, 133113 (2013).
15. Jin, Z. *et al.* A Revisit to High Thermoelectric Performance of Single-layer MoS_2. *Sci. Rep.* **5**, 18342 (2015).
16. Mak, K. F., Lee, C., Hone, J., Shan, J. & Heinz, T. F. Atomically thin $MoS_{(2)}$: a new direct-gap semiconductor. *Phys. Rev. Lett.* **105**, 136805 (2010).
17. Cheiwchanchamnangij, T. & Lambrecht, W. R. L. Quasiparticle band structure calculation of monolayer, bilayer, and bulk MoS_2. *Phys. Rev. B* **85**, 205302 (2012).
18. Lin, Y. C. *et al.* Properties of Individual Dopant Atoms in Single-Layer MoS_2: Atomic Structure, Migration, and Enhanced Reactivity. *Adv. Mater.* **26**, 2857 (2014).
19. Cheng, Y. C., Zhu, Z. Y., Mi, W. B., Guo, Z. B. & Schwingenschlögl, U. Prediction of two-dimensional diluted magnetic semiconductors: Doped monolayer MoS_2 systems. *Phys. Rev. B* **87**, 100401 (2013).
20. Ramasubramaniam, A. & Naveh, D. Mn-doped monolayer MoS_2: An atomically thin dilute magnetic semiconductor. *Phys. Rev. B* **87**, 195201 (2013).
21. Feng, N. *et al.* First principles prediction of the magnetic properties of $Fe-X_{(6)}$ (X = S, C, N, O, F) doped monolayer $MoS_{(2)}$. *Sci. Rep.* **4**, 3987 (2014).
22. Yun, W. S. & Lee, J. D. Unexpected strong magnetism of Cu doped single-layer $MoS_{(2)}$ and its origin. *Phys. chem. chem. phys.* **16**, 8990–8996 (2014).
23. Lembke, D., Allain, A. & Kis, A. Thickness-dependent mobility in two-dimensional $MoS_{(2)}$ transistors. *Nanoscale* **7**, 6255–6260 (2015).
24. Zhou, C. *et al.* Low voltage and high ON/OFF ratio field-effect transistors based on CVD MoS_2 and ultra high-k gate dielectric PZT. *Nanoscale* **7**, 8695–8700 (2015).
25. Ghatak, S., Pal, A. N. & Ghosh, A. Nature of Electronic States in Atomically Thin MoS_2 Field-Effect Transistors. *Acs. Nano.* **5**, 7707–7712 (2011).
26. Qiu, H. *et al.* Electrical characterization of back-gated bi-layer MoS_2 field-effect transistors and the effect of ambient on their performances. *Appl. Phys. Lett.* **100**, 123104 (2012).
27. Bao, W., Cai, X., Kim, D., Sridhara, K. & Fuhrer, M. S. High mobility ambipolar MoS_2 field-effect transistors: Substrate and dielectric effects. *Appl. Phys. Lett.* **102**, 042104 (2013).
28. Li, H. *et al.* Fabrication of Single- and Multilayer MoS_2 Film-Based Field-Effect Transistors for Sensing NO at Room Temperature. *Small* **8**, 63–67 (2012).
29. Leong, W. S. *et al.* Tuning the threshold voltage of MoS_2 field-effect transistors via surface treatment. *Nanoscale* **7**, 10823–10831 (2015).
30. Radisavljevic, B., Whitwick, M. B. & Kis, A. Integrated circuits and logic operations based on single-layer MoS_2. *ACS nano* **5**, 9934 (2011).
31. Gourmelon, E. *et al.* MS_2 (M = W, Mo) photosensitive thin films for solar cells. *Sol. Energy Mater. Sol. Cells* **46**, 115 (1997).
32. Brandbyge, M., Mozos, J.-L., Ordejón, P., Taylor, J. & Stokbro, K. Density-functional method for nonequilibrium electron transport. *Phys. Rev. B* **65**, 165401 (2002).
33. Soler, J. M. *et al.* The SIESTA method for *ab initio* order-*N* materials simulation. *J. Phys.: Condens. Matter.* **14**, 2745–2749 (2002).
34. Taylor, J., Guo, H. & Wang, J. Ab initio modeling of quantum transport properties of molecular electronic devices. *Phys. Rev. B* **63**, 245407 (2001).
35. Perdew, J. P., Burke, K. & Ernzerhof, M. Generalized Gradient Approximation Made Simple. *Phys. Rev. Lett.* **77**, 3865–3868 (1996).
36. Büttiker, M., Imry, Y., Landauer, R. & Pinhas, S. Generalized many-channel conductance formula with application to small rings. *Phys. Rev. B* **31**, 6207–6215 (1985).
37. Zou, F., Zhu, L., Gao, G. Y., Wu, M. H. & Yao, K. L. Temperature-controlled spin filter and spin valve based on Fe-doped monolayer MoS_2. *Phys. Chem. Chem. Phys.* **18**, 6053–6058 (2016).

Acknowledgements

Author Contributions

L.Z. and F.Z. designed the two-probe system and performed the numerical calculation. L.Z. analyzed the results and wrote the manuscript. K.L.Y. and G.G. supervised the whole work. All authors reviewed the manuscript.

Additional Information

Competing Interests: The authors declare that they have no competing interests.